ACS APPLIED MATERIALS & INTERFACES

www.acsami.org

Research Article

# Unique MIL-53(Fe)/PDI Supermolecule Composites: Z-Scheme Heterojunction and Covalent Bonds for Uprating Photocatalytic Performance

Hui Chen,[⊥] Wengao Zeng,[⊥] Yutang Liu,* Wanyue Dong, Tao Cai, Lin Tang,* Juan Li, and Wenlu Li

Cite This: https://doi.org/10.1021/acsami.1c01308

Read Online

ACCESS | Metrics & More | Article Recommendations | Supporting Information



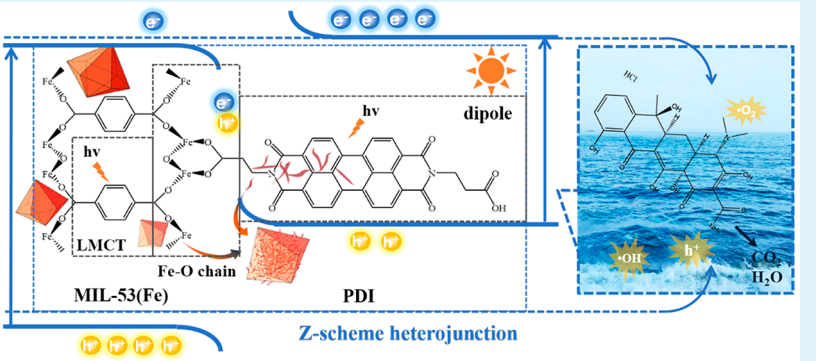


**ABSTRACT:** It is important to find an effective way to enhance the photocatalytic efficiency of metal−organic frameworks. In this work, an organic supermolecule perylene diimide (PDI) semiconductor with a carboxyl terminal was added into the synthesis process of MIL-53(Fe) crystals. The PDI/MIL-53(Fe) (PM) composite photocatalyst was first obtained. The TC-H photodegradation rate of the most efficient 5PM was nearly 94.08% within 30 min, whose apparent reaction rate constant ($k$) is 4 times that of PDI and 33 times that of MIL-53(Fe), respectively. By investigation and characterization, it has been found that PDI nanofibers were dispersed and fixed in MIL-53(Fe) and bonded to each other by covalent bonds. The radical trap experiments and electron spin resonance analysis illustrated that hydroxyl radical (·OH), superoxide radical ($\cdot O_2^-$), and photogenerated holes ($h^+$) were active species. Combined with the band structure of PDI and MIL-53(Fe), it is proposed that the PM photocatalyst was a Z-scheme heterojunction mechanism. Therefore, PM photocatalysts showed excellent charge separation and transfer ability. The performance improvement of 5PM is due to enhanced visible light absorption, efficient charge separation, and excellent redox potential. Five cyclic photocatalytic tests and experiments further demonstrate that the 5PM photocatalyst has a promising future for pollutant removal.

**KEYWORDS:** *PDI, MIL-53(Fe), photocatalytic degradation, Z-scheme heterojunction, covalent bond*

## 1. INTRODUCTION

The pollution situation of antibiotics in the environment is now getting worse. Tetracycline (TC) antibiotic pollution is becoming a worldwide environmental issue for the solubility, stabilization, and high toxicity.[1] Effective methods must be taken to address this environmental problem. In many physical[2] or chemical methods,[3] photocatalytic degradation as an effective, energy-saving, and economical pollution processing mode attracted much more attention.[4] Photocatalysts convert solar energy to chemical energy of redox reactions and generate activity species with water and dissolved oxygen separately, which can effectively remove contaminants from the water or convert contaminants into environmentally friendly substances.[5−7] The improvement of photocatalyst performance is the key target of exploration. An excellent photocatalyst would promote the practical application of photocatalytic wastewater processing.[8] It has been reported that increasing the light absorption, the active site, and the photogenerated charge separation of photocatalysts are three effective methods to improve the efficiency of photocatalysis.

Metal−organic frameworks (MOFs), a kind of crystalline material composed of metal nodes and organic linking ligands, are gaining prominence because of their ordered porous framework, coordinated structur, and high specific surface

Received: January 20, 2021
Accepted: March 22, 2021

area.[9] In recent years, MOFs have been widely studied in the fields of photocatalysis,[10] catalysis, adsorption,[11,12] catalytic oxidation,[13] gas storage,[14] and so on. The MOFs obtained by specially designing with different ligands and nodes can meet the needs of different fields. In terms of photocatalysis, some photocatalytic MOFs materials, such as MILs and UiOs, have the advantages of good stability, UV−visible light absorption, and relatively strong photocatalytic oxidation ability.[15] However, weak visible light absorption, rapid recombination rate of the photogenerated electron−hole pairs, and insufficient degradation efficiency still remain challenges in the bare MOFs photocatalysts.[16] For above disadvantages, it has been demonstrated that some methods such as constructing a heterojunction, metal loading, and framework adjustment were beneficial to increasing the performance of MOFs photocatalysts.[17] The construction of a heterojunction is an effective method for enhancing charge migration and transfer and inhibiting the recombination of photogenerated electron−hole pairs. Besides, the combination of MOFs materials and other photocatalysts is a potential strategy as its good performance of adsorbability. Looking for an excellent heterojunction structure has a profound impact on the development of MOFs photocatalytic materials.[18] In the process of MOFs synthesis, the addition of foreign particles such as impurities, bubbles, or solid particles is considered to cause the nucleation and the growth of MOFs on these particle interfaces.[19] Therefore, using an opportune photocatalytic semiconductor material as foreign particles of MOFs is conducive to constructing heterojunction structures with large contact areas and tight interfaces.

Meanwhile, with the development of organic photocatalytic PDI (perylene-3,4,9,10-tetracarboxylic diimide) as an n-type organic supramolecular semiconductor was beginning to come into focus due to its high stability and excellent optical property. Recently, Zhu et al. reported its derivative, supramolecular nanofibers of *N*,*N*′-di(propanoic acid)-perylene-3,4,9,10-tetracarboxylic diimide, which introduces a terminal carboxyl group at the imides of PDI to make it have higher photocatalytic activity and stability.[20] In addition, these PDI supramolecular nanofibers (hereinafter called PDI) show broad-spectrum light absorption and strong oxidizing power for organic pollutants degradation. The high stability of PDI was suitable for the reaction conditions of MOFs synthesis with high-temperature and polar organic solvents.[21] Moreover, a PDI nanofiber is a nanorod with a diameter of ∼20−50 nm and a length of ∼0.8−1.2 μm, which is smaller than most MOFs photocatalysts.[22] Besides, some special terminus (−COOH or −OH) at the molecular interfaces can force the oriented attachment of crystal growth materials. It has been reported that the carboxyl terminal (−COOH) mimics the carboxylic acid organic linker (1,3,5-benzenetricarboxylate (BTC), 1,4-benzenedicarboxylic acid (BDC), and so on) to capture metal ions in the open framework structure.[23] In conclusion, a PDI nanofiber equipping with a carboxyl terminal, relatively small size, and excellent stability can be chosen to form an excellent heterojunction with MOFs.

Fe-based MOFs were easy to prepare and environmentally friendly and have been more studied in the field of photocatalytic degradation of pollutants.[24] Both MIL-88(A)[25] and MIL-53(Fe)[26] have been reported that the efficiency of photocatalytic degradation of pollutants can be improved by combining with two-dimensional materials to form an excellent heterojunction. Among them, MIL-53(Fe) has a narrow band gap, which can absorb the solar energy in visible wavelengths. Therefore, in this study, the PDI/MIL-53(Fe) (PM) photocatalyst was first reported. The dispersed PDI nanofibers were put into the precursor solution of synthetic MOFs. Then, the heterogeneous mixed material of MIL-53(Fe) and PDI could be obtained by a simple one-step thermal method. The PM composites have a unique hairball structure and grow together with dispersive PDI as the inner part. Besides, the large contact surface enhanced the charge transfer between heterogeneous junctions. The as-prepared PM composites showed excellent performance in the tetracycline hydrochloride (TC-H) photodegradation. The photodegradation rate of 5PM was 33 times that of MIL-53(Fe) and 4 times that of PDI, respectively. The PM photocatalysts were analyzed and investigated by analysis characterization techniques. It has been found that PDI nanofibers were dispersed and fixed in MIL-53(Fe) and bonded to each other by covalent bonds. The introduction of PDI effectively enhances the migration of photoelectrons through the phase-interface boundaries due to the good interfacial contact effect, which subsequently improves the photocatalytic performance of pollutant degradation. The radical trap experiments and electron spin resonance (ESR) analysis illustrated that hydroxyl radical (·OH), superoxide radical ($\cdot O_2^-$), and photogenerated holes ($h^+$) were active species. Combined with the band structure of PDI and MIL-53(Fe), it is proposed that the PM photocatalyst was a Z-scheme heterojunction mechanism, which accelerates the charge separation and transfer in composites, as well as provides the profitable redox potential for the strong degradation ability under illumination.

## 2. EXPERIMENT

**2.1. Chemicals.** $FeCl_3·6H_2O$, 1,4-benzenedicarboxylic acid (1,4-BDC), *N*,*N*-dimethylformamide (DMF), triethylamine ($C_6H_{15}N$), tetracycline hydrochloride (TC-H), methanol ($CH_4O$), and ethanol ($C_2H_6O$, 99.7%) were all purchased from Sinopharm Chemical Reagent Co. Ltd. Perylene-3,4,9,10-tetracarboxylic dianhydride ($C_{24}H_8O_6$, 98%), imidazole ($C_3H_4N_2$, 99%), and β-alanine ($C_3H_7NO_2$, 99%) were all purchased from Aladdin. The water used in this study for the preparation of all solutions was prepared by an ULUPURE purification system. All the chemical reagents were used directly without further purification.

**2.2. Synthesis of PDI Nanofibers.** The method for synthesizing PDI nanofibers refers to previous studies.[20] The mixtures of perylene-3,4,9,10-tetracarboxylic dianhydride (1.376 g), β-alanine (2.5 g), and imidazole (18 g) were heated at 100 °C for 4 h under the protection of argon. After cooling to room temperature, the product was incorporated into the mixed solution of 100 mL of ethanol and 300 mL of hydrochloric acid (2 M) and stirred overnight. Then 834 μL of triethylamine solution was added and stirred until the mixed solution turned red; the addition of 27.3 mL of 4.0 M HCl is used for the formation of PDI supermolecules. The suspension was collected by centrifugation and washed with deionized water until the pH of the centrifugal supernatant turned to be neutral and finally dried at 60 °C for 12 h to afford PDI nanofibers.

**2.3. Synthesis of Composite Photocatalysts.** The composite photocatalysts of MIL-53(Fe) and PDI were synthesized using a solvothermal method referred to in a previous reported.[27] 5 mg of PDI nanofibers was dispersed in 25 mL of DMF solution by ultrasound. Then terephthalic acid ($H_2BDC$, 5 mmol) and ferric chloride hexahydrate ($FeCl_3·6H_2O$, 5 mmol) were added to the mixture and stirred for 30 min. Then the well-mixed solution was transferred to a Teflon-lined pressure vessel (50 mL) and heated at 150 °C for 5 h. Finally, the product was collected by centrifugation and washed with methanol. The collected product was immersed in methanol for 12 h to remove DMF from pores and dried at 60 °C for


https://doi.org/10.1021/acsami.1c01308
ACS Appl. Mater. Interfaces XXXX, XXX, XXX−XXX

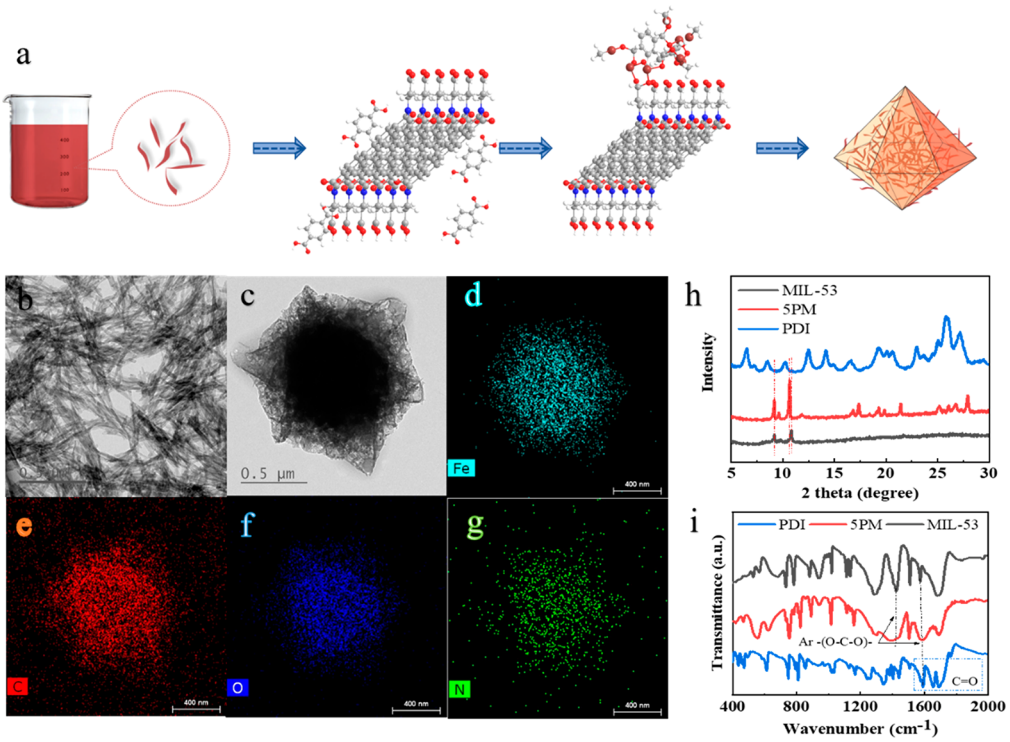


**Figure 1.** (a) The generation process of the composite sample. (b, c) The TEM images of PDI and 5PM. (d−g) The elemental mapping images of 5PM. (h) The X-ray diffaction (XRD) of samples. (i) The FT-IR spectra of samples.

12 h to get the final product, named 5PM. The same method with different addition of PDI nanofibers (2.5, 10, and 15 mg) was used for preparing materials, which are named 2.5PM, 10PM, and 15PM, respectively. The process diagram of sample preparation is shown in Figure S1.

**2.4. Characterization.** Morphologies and structures of the prepared materials were observed by field-emission scanning electron microscopy (FESEM, Hitachi, S-4800) and transmittance electron microscopy (TEM, JEOL, JEM-2100F). The crystal structures of the samples were determined by X-ray diffraction (XRD, Rigaku, Smartlab) at a scanning rate of 5 $min^{-1}$ in the $2\theta$ range of 5−80°, and chemical composition characterizations of as-prepared samples were determined by X-ray diffraction, and X-ray photoelectron spectroscopy (XPS, Thermo Fisher Scientific, England), in which the binding energies of samples were calibrated with respect to the adventitious carbon (C 1s) as a reference line at 284.8 eV.

The ultraviolet visible (UV−vis) diffuse-reflectance spectra (DRS) were recorded by using a UV−vis spectrophotometer (Cary 300, Varian) in the wavelength range from 200 to 800 nm with $BaSO_4$ as the reference. The steady-state photoluminescence (PL) spectra were collected on a HitachiF-7000 fluorescence spectrophotometer at the excitation wavelength of 350.0 nm. The time-resolved photoluminescence (TRPL) spectra were collected on an FS5 fluorescence spectrophotometer (Edinburgh Instruments, U.K.), with the excitation wavelength at 350.0 nm.

**2.5. Electrochemical Measurements.** Electrochemical measurements were measured by a CHI 660C electrochemical analyzer (CHI Inc., USA) with a typical three-electrode configuration in 0.1 M $Na_2SO_4$ solution. A saturated calomel electrolyte was used as a reference electrode, and a Pt coil was used as a counter electrode. The working electrode prepared by as-prepared materials thin film on fluorine-doped tin oxide (FTO) used Nafion as the adhesive. The response of the photocurrent was measured under a 300 W Xe lamp with the 420 nm cutoff filter. Other electrochemical measurements were recorded without illumination. Electrochemical impedance spectra (EIS) were obtained in the frequency range of 100 00−0.01 Hz with and without visible light irradiation.

**2.6. Evaluation of Catalytic Ability.** Photocatalytic ability of the composite photocatalyst was evaluated through the photodegradation experiment under visible light irradiation. Typically, 5 mg of as-prepared powder was added into the reaction solution (25 mL, 20 mg/L TC-H). The suspension was stirred for 30 min under a dark environment to reach an adsorption-desorption equilibrium. After visible light illumination, which was generated by a 300 W Xe lamp with a 420 nm cutoff filter, 1 mL of suspension was taken out at a given interval time and separated through a 0.22 $\mu$m filter membrane (hydrophobic membranes). All the concentrations of the reactant that remained in the filtrate were analyzed by a UV−vis spectrophotometer (UV-2600).

## 3. RESULTS AND DISCUSSION

**3.1. Characterization of Morphology, Crystal, and Chemical Structures.** In the process of crystallization, different environments will affect the crystal morphology of MOFs.[28] The final morphology of MIL-53(Fe) was affected by different quantities of PDI nanofibers in the precursor solution. According to the pictures of FESEM (Figures S2 and S3) and TEM (Figure S4), it can be seen that the shape of MOFs gradually becomes plump, which changes from a concave octahedron to a dodecahedron with the gradual addition of PDI. The morphology of bare PDI is a slender, flakelike nanofiber that resembles a willow leaf in shape. It indicates that PDI nanofibers may play an active role in nucleation and growth of MIL-53(Fe). The generation process of the composite photocatalyst is shown in the Figure 1a. The dispersed PDI fibers act as the introduced micro-impurity in the liquid-phase of MIL-53(Fe). Fe ions would be attracted to the terminal carboxyl group on PDI by the electrostatic attraction.[29] Then MOFs gradually grew and wrapped around the PDI. It can be seen clearly in TEM (Figure 1b,c) that the surface of 5PM is very rough and uneven due to the integration of PDI nanofibers. Also, Figure 1d−g shows the elemental


https://doi.org/10.1021/acsami.1c01308
ACS Appl. Mater. Interfaces XXXX, XXX, XXX−XXX

mapping images of 5PM. From these graphs, it can be seen that all the elements (C, N, O, and Fe) are distributed evenly in 5PM, indicating that PDI is uniformly dispersed in MIL-53(Fe) and has a large contact surface with MIL-53(Fe). Therefore, this heterogeneous junction structure would provide a large contact area between them, which is beneficial to facilitating the transfer of charge in the heterojunction.[30]

The specific surface area and porous structures are key parameters of photocatalyst, which can be determined by the $N_2$ adsorption-desorption measurement. Meanwhile, the pore distribution curves of the as-prepared photocatalysts are calculated by DFT. The data and analysis results of BET have been supplemented at Figure 2 and Table 1. The

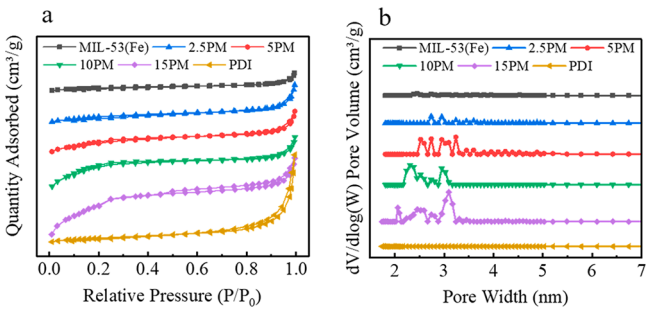


**Figure 2.** $N_2$ adsorption-desorption isotherms (a) and pore size distribution (b) of composites.

**Table 1. Physicochemical Parameters of the Photocatalysts**

| samples | BET ($m^2$/g) | $V$ ($cm^3$/g) | $D$ (nm) |
|---|---|---|---|
| MIL-53(Fe) | 17.8211 | 0.0303 | 2.38−4.88 |
| 2.5PM | 62.2371 | 0.077 | 2.73−4.88 |
| 5PM | 137.2334 | 0.146 | 2.52−4.88 |
| 10PM | 146.8014 | 0.103 | 2.24−3.09 |
| 15PM | 344.1046 | 0.226 | 2.06−3.45 |
| PDI | 24.9177 | 0.139 | no microporous |

isotherms of MIL-53(Fe), 2.5PM, 5PM, 10PM, and 15PM are type-IV $N_2$ adsorption curves. The BET surface area of PM composites increases from 17.82 $m^2$/g of MIL-53(Fe) to 344.10 $m^2$/g of 15PM with the increase of PDI dose. The isotherms of PDI show a type-III $N_2$ adsorption curve with the lowest adsorption surface area. In addition, the isotherms of 15PM exhibit an obvious H4 hysteresis loop, which indicates that an excessive dose of PDI is contributing to the existence of some slits in the PM. It can be seen from the pore size distribution curve that the embedding of PDI nanofibers increases the micropores in MIL-53(Fe). The increased specific surface area provides more active sites and reaction interfaces for catalysis. The existence of mesopores and micropores accelerates the substance transferring.

The crystal structures of samples (Figure 1h) were measured by X-ray diffraction (XRD). In the XRD pattern of the composite sample (5PM), the characteristic diffraction peaks corresponding to MIL-53(Fe) were observed around 9.2° and 10.8°.[31] Self-assembled PDI nanofibers have weak diffraction peaks ranging from 5° to 30° due to poor crystallinity.[32] The corresponding peak of PDI is non-obvious in the pattern of 5PM, because PDI is small and wrapped in the MIL-53(Fe). Besides, some new diffraction peaks significantly appeared between 15° and 35° in the pattern of 5PM due to the addition of PDI. It indicates that the crystallization of MIL-53(Fe) changed partially to form 5PM which was a composite with a similar structure.[33] The FT-IR spectra were employed here to analyze organic functional groups. As shown in Figure 1i, PDI-based samples have three distinct characteristic peaks in 1691 and 1652 $cm^{-1}$, corresponding to C═O and C═C stretching vibrations (blue dashed outline in Figure 1i), which appears in both PDI samples.[32] Also, MIL-53(Fe) in 1691 $cm^{-1}$ has the peak of the stretching vibration of C═O, because BDC and PDI all have a similar carboxyl structure. It deduces that the metal nodes can also bind on PDI in a similar way to BDC. In the FT-IR spectra of MIL-53(Fe), there are two peaks at 1577 and 1423 $cm^{-1}$ that are assigned to asymmetric ($\nu_{as}$(C-O)) and symmetric ($\nu_s$(C-O)) dicarboxylate vibrations of carboxyl groups, respectively, proving the existence of dicarboxylate ligands.[34] It can be found by comparison that the FT-IR spectra of 5PM and MIL-53(Fe) are similar, indicating that 5PM maintains the original framework structure of MIL-53(Fe). Meanwhile, the wavenumber of C═O blue-shifts from 1573 $cm^{-1}$ at MIL-53(Fe) to 1585 $cm^{-1}$ at 5PM (Figure S5), further confirming that the PDI participates in the synthesis of 5PM by the bidentate coordination of the carboxylate group with the iron clusters in MIL-53(Fe).[27,35] Thus, in addition to adsorption binding, the in situ binding method of MIL-53(Fe) and PDI also has covalent bonding. Different connection methods would affect the charge transfer between material interfaces and need to be further studied and analyzed. Chemical bonding between materials can stabilize heterogeneous structures and promote charge transfer between interfaces.

Therefore, X-ray photoelectron spectroscopy (XPS) was used to confirm the surface structure of elements and the interaction of MIL-53(Fe) and PDI in composites.[36] By observing the survey XPS spectra of 5PM and MIL-53(Fe) (Figure 3a), it can be found that there are C 1s, O 1s, and Fe 2p peak signals in the composite material. The obvious N 1s signal only appears at 5PM, which proves the existence of PDI in the composite material. The high-resolution XPS (HRXPS) spectra of different elements are treated with separate peaks

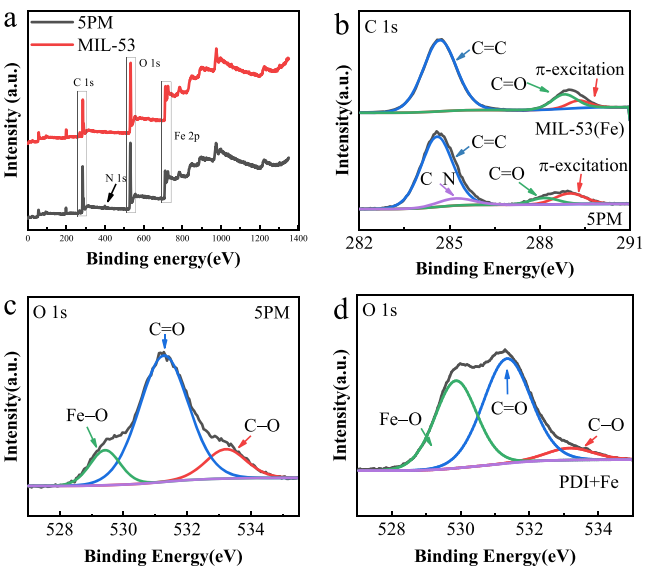


**Figure 3.** (a) The survey XPS of 5PM and MIL-53(Fe), (b) the high-resolution XPS (HRXPS) C 1s spectrum 5PM and MIL-53(Fe), (c, d) high-resolution XPS (HRXPS) O 1s spectrum of 5PM and PDI-Fe.


https://doi.org/10.1021/acsami.1c01308
ACS Appl. Mater. Interfaces XXXX, XXX, XXX−XXX

shown in Figure 3b,c. It can be seen from C 1s patterns of 5PM and MIL-53(Fe) that the corresponding peak signals of C═C, C═O, and $\pi$-excitation are 284.7, 288.3, and 289.2 eV, respectively. Besides, only the pattern of 5PM shows a C-N signal peak around 285.3 eV. The O 1s pattern of 5PM in Figure 3c indicated the existence of Fe-O, C═O, and C-O in the materials, corresponding to 529.4, 531.2, and 533.2 eV, respectively. In order to prove the connection between PDI and MIL-53(Fe), PDI-Fe was prepared under the same reaction conditions as those of 5PM. PDI-Fe was synthesized from PDI and $Fe^{3+}$ only and characterized. The peak signals of Fe-O are also found in the O 1s pattern of PDI-Fe (Figure 3d). It proved the chemical bond between PDI and Fe could be generated under the same synthetic conditions as those of MIL-53(Fe). The joint point where MIL-53(Fe) covalently bonds with PDI was the iron-oxygen cluster. The binding energy of Fe 2p patterns showed that the Fe element exists only in the form of Fe-$O_\chi$ at 5PM and MIL-53(Fe). The chemical bond composition between PDI and MIL-53(Fe) can be briefly shown in Figure S6.

**3.2. Performance Testing of Photocatalytic Degradation.** The photocatalytic degradation activities of the as-prepared samples were studied under the irradiation of visible light ($\lambda \geq 420$ nm) using 20 mg/L TC-H as the target pollutant. Before irradiation, the suspension of all samples was ultrasonically dispersed and stirred for 30 min to reach an adsorption-desorption equilibrium (Figure S7). Control experiments showed that TC-H would not be degraded under light illumination in the absence of photocatalysts. In Figure 4, the TC-H degradation rates within 30 min after

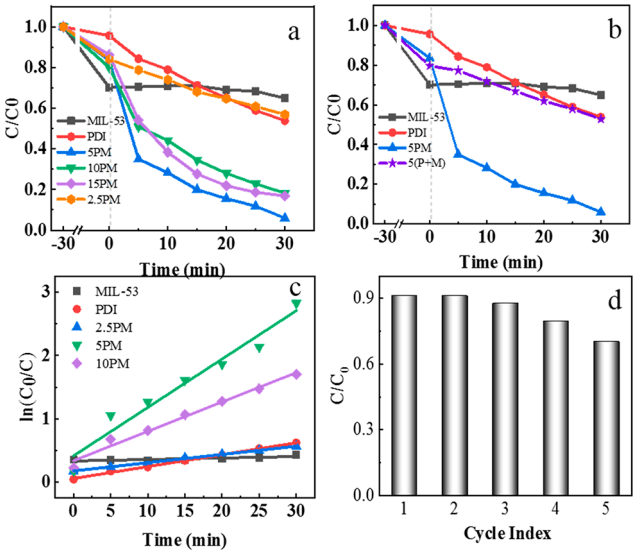


**Figure 4.** (a, b) The TC-H photodegradation rates of different samples. (c) The corresponding photodegradation kinetics of TC-H with different samples. (d) Photodegradation of TC-H for 5-cycles using 5PM.

illumination in the presence of MIL-53(Fe), PDI, 2.5PM, 5PM, 10PM, and 15PM were compared, respectively. It can be seen that the degradation efficiency of 5PM is the best, which can remove TC-H with an efficiency of nearly 94.08% within 30 min, followed by 10PM with the TC-H removal rates of 81.80%. Moreover, the photodegradation effects of pure MIL-53(Fe) and PDI were relatively poor, with only 35.08% and 46.15% of TC-H removed within 30 min, respectively. The apparent reaction rate constants ($k$) of photocatalytic degradation of TC-H were calculated by the pseudo-first-order equation,[37] and the result is shown in Figure 4c. In addition, the apparent reaction rate constants ($k$) of the MIL-53(Fe), PDI, 2.5PM, 5PM, and 10PM are calculated to be 0.00229, 0.01882, 0.01301, 0.07647, and 0.04641 $min^{-1}$, respectively. Comparing with the $k$ of monomer MIL-53(Fe) or PDI, it can be found that the performance of composite samples has been significantly improved. The TC-H photodegradation rate of 5PM is 4 times that of PDI and 33 times that of MIL-53(Fe), respectively. At the same time, the degradation performance of the sample (named 5(P+M)) prepared by physical mixing MIL-53(Fe) and PDI with an equal proportion of 5PM was only 46.07% (Figure 4b). Besides, it can be found through the 5-cycle test on 5PM (Figure 4d) that the TC degradation rate decreased slightly from 91.13% to 69.98%, which indicates that the composite material has good stability. The XPS, XRD, FT-IR, and SEM of photocatalysts before and after the cycling experiment are shown in Figures S8 and S9. The results of XRD (Figure S8b) show that there is no significant change in the crystal phase and structure of the photocatalysts after the cycling experiment, which proves that the photocatalysts have good stability. For the comparison of XPS spectra (Figure S8a) before and after the cycling experiment, the authors selected the most representative Fe 2p patterns of samples. The high-resolution XPS (HRXPS) of 5PM and used 5PM showed that the reduction of Fe in the photocatalyst occurred after the cycling experiment, which was related to the photoreduction corrosion of the Fe-based MOFs photocatalyst in previous studies. Different batches of PM photocatalyst have slightly different morphologies. Also, the FT-IR spectra will be affected by different testing apparatus and environments. In order to ensure the consistency of the comparison of the FT-IR spectra and SEM, the author reprepared the photocatalysts and re-measured the FT-IR spectra and SEM with the same instrument. As shown in Figure S9, the 5PM can maintain its morphology well after the cycling experiment. The comparison in the FT-IR spectra (Figure S8c) shows that the functional groups of the 5PM have changed due to the adsorption and degradation of pollutants. But the characteristic peak value of the main functional group has not changed, which proves that the composition of the functional group on the 5PM surface remains stable.

Meanwhile, the influence of inorganic salts on photocatalytic degradation was tested. The experimental results showed in Figure S10 that the presence of inorganic salts ($CaCl_2$, $NaHCO_3$, $Mg(NO_3)_2$, $K_2SO_4$) has no obvious effect on photocatalytic performance. It was not for nothing that photocatalyst performance was improved. Here is an analysis from three "E" aspects: Enhanced visible light absorption, Efficient charge separation and transfer, and Excellent redox potential.

**3.3. Optical Absorption Properties of Photocatalysts.** Most of the energy of sunlight is concentrated in visible light. The better the performance of visible light absorbing photocatalysts, the more photogenerated charge it can generate. The absorption capacity was determined by the band structure of the photocatalyst. The band structure mainly consists of the band gap ($E_g$), the conduction band potentials ($E_{CB}$), and the valence band potential ($E_{VB}$), in which the sum of $E_{CB}$ and $E_g$ is the value of $E_{VB}$.[38] Therefore, the UV−vis diffuse reflectance spectra (UV−vis DRS) were used to


https://doi.org/10.1021/acsami.1c01308
ACS Appl. Mater. Interfaces XXXX, XXX, XXX−XXX

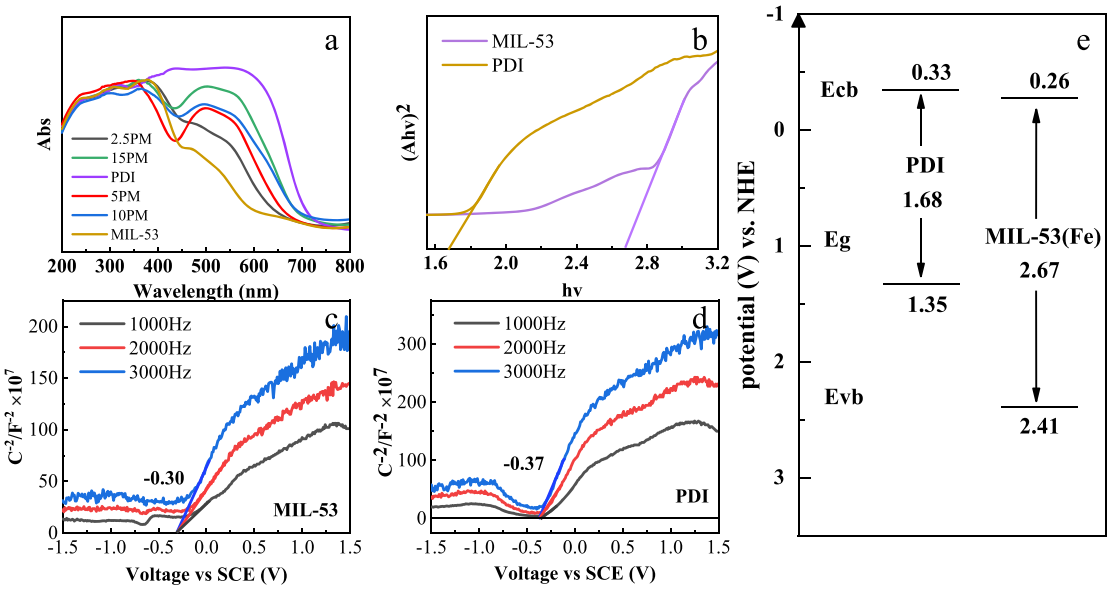


**Figure 5.** (a, b) The UV−vis diffuse reflectance spectra of samples and the corresponding Tauc's plots. (c, d) Mott−Schottky plot of MIL-53(Fe) and PDI. (e) The band structure data of materials.

investigate the optical properties of as-prepared samples. Figure 5a shows the light absorption value of MIL-53(Fe), PDI, 2.5PM, 5PM, 10PM, and 15PM with the wavelength from 200 to 800 nm. It can be seen that PDI has good visible light absorption. The absorption edge of PDI was around 700 nm, and the absorption edge of MIL-53(Fe) was around 600 nm. After introducing PDI, the composite samples revealed new absorption peaks from 450 to 700 nm. Meanwhile, the absorption value increased with the increase of PDI dose, proving that adding PDI into MIL-53(Fe) has broadened the visible light absorption range of materials. The $E_g$ values of samples were determined by the Kubelka−Munk method. As shown in Figure 5b, the $E_g$ values of MIL-53(Fe) and PDI were estimated to be about 2.67 and 1.68 eV, respectively.[22,39] In general, the $E_{CB}$ of an n-type semiconductor is about minus 0.2 V than the flat band potential ($E_{fb}$). Then the $E_{fb}$ of the semiconductor was measured by the Mott−Schottky plot method,[40] which is shown in Figure 5c,d. The conversion formula of a saturated calomel electrode (SCE) and a normal hydrogen electrode (NHE) was: $E_{NHE} = E_{SCE} + 0.24$. The $E_{fb}$ of MIL-53(Fe) and PDI were −0.30 and −0.37 V versus the SCE, and the corresponding $E_{CB}$ were −0.26 and −0.33 V versus the NHE, respectively. All the band structure data of materials can be calculated from the above content, shown in Figure 5e.

**3.4. Photoelectrochemical Properties of Photocatalysts.** The recombination of photogenerated charge in a photocatalyst has also been a problem. Effective charge separation can provide more operative charge instead of turning into heat energy or fluorescence emission in the process of recombination. The main way to separate charges is to form an internal or external polarization field, for instance, forming a heterojunction. The steady-state photoluminescence (PL) can measure the fluorescence intensity produced by a semiconductor after photoexcitation. The fluorescence data of samples are shown in Figure 6a,b. At the same excitation wavelength, both MIL-53(Fe) and PDI were excited to produce emission fluorescence at different wavelength ranges of 420−600 nm and 620−720 nm, respectively. In the 420−

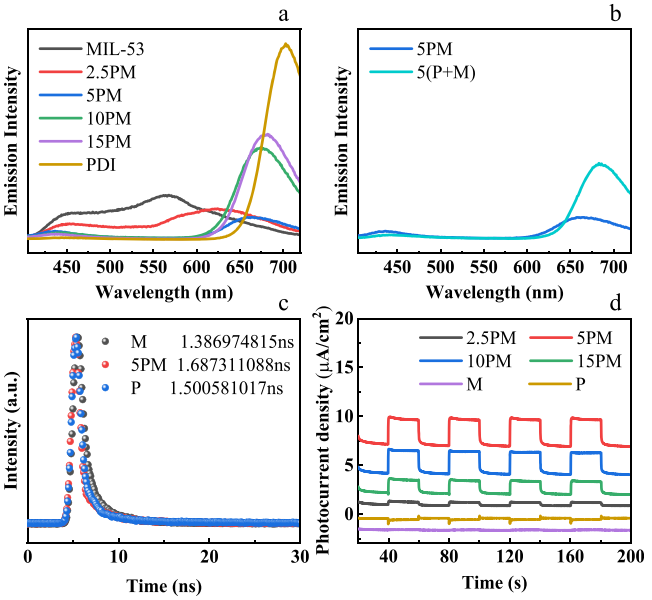


**Figure 6.** (a, b) The steady-state photoluminescence (PL) of samples. (c) The time-resolved photoluminescence (TRPL). (d) The photocurrent test.

600 nm emission fluorescence range, the fluorescence intensity significantly decreased with the gradual increase of PDI, proving that the addition of PDI would reduce the charge recombination of the composites by separating the photogenerated charges on the MIL-53(Fe). Meanwhile, in the 620−720 nm emission fluorescence range, only the lowest fluorescence intensity was found in the 5PM, indicating that the charge recombination in PDI was maximally inhibited at 5PM. Furthermore, the fluorescence intensities of 5(P+M) and 5PM all are weak in 420−600 nm, proving that no matter the physical mixing sample or composite sample, the addition of PDI can make charge separation on MIL-53(Fe). It proves that the addition of PDI can make improved charge separation on MIL-53(Fe) in the form of both physical mixing sample and heterojunction sample. However, in 620−720 nm, the


https://doi.org/10.1021/acsami.1c01308
ACS Appl. Mater. Interfaces XXXX, XXX, XXX−XXX

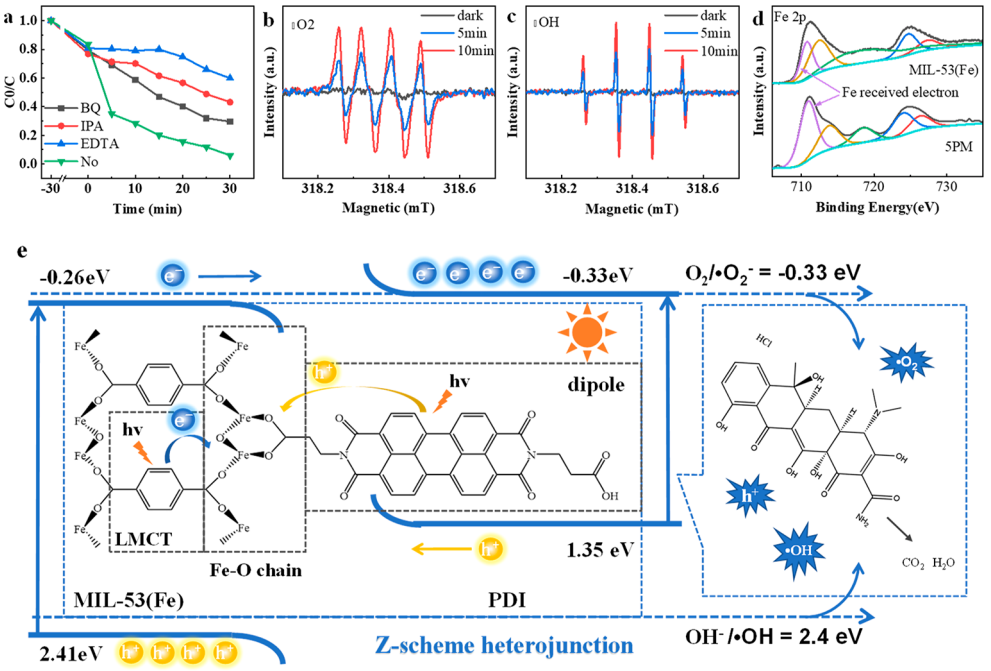


**Figure 7.** (a) The radical trap experiments. (b, c) Electron spin resonance (ESR) spectra of DMPO-·OH and DMPO-·$O_2^-$. (d) The high-resolution XPS (HRXPS) spectra of 5PM and MIL-53(Fe). (e) Photocatalytic mechanism of 5PM composite.

fluorescence excitation of 5PM was significantly weaker than 5(P+M), which indicated that the 5PM heterojunction plays a strong role on promoting charge separation on PDI. This is mainly because PDI was closely bounded to MIL-53(Fe) and highly dispersed in the composite.

In addition, time-resolved photoluminescence (TRPL) monitored at the corresponding emission peaks of PL revealed the lifetime of the recombining photogenic charges in different materials (Figure 6c). The PL decay curve was fitted with a triexponential equation (E S1). The relevant component's emission lifetimes and corresponding amplitudes are listed in Table S1: where B1, B2, and B3 represent the normalized amplitudes of each decay component. $\tau$1, $\tau$2, and $\tau$3 are values of the lifetime components, respectively.[41] Figure 6c displays the PL lifetime decay curves of MIL-53(Fe), 5PM, and PDI. The PL lifetime of 5PM was 1.69 ns, longer than that of PDI (1.50 ns) and MIL-53(Fe) (1.39 ns). It was further proved that the composite material 5PM has better performance of charge separation than MIL-53(Fe) and PDI. This conclusion is also reflected in the photocurrent test (Figure 6d). The intensities of the photocurrent, in order, were 5PM, 10PM, 15PM, 2.5PM, PDI, and MIL-53(Fe), which was nearly consistent with the performance ranking in the photodegradation experiment. The EIS was also measured, and the results are shown in Figure S11. The arc radius of EIS Nyquist plots of the bare catalysts varies greatly between MIL-53(Fe) and PDI. The PM composites have a small arc radius because of the presence of MIL-53(Fe). According to the arc radius of different composites in EIS, it is found that the PM composites with the highest and lowest PDI doses had a greater arc radius, followed by 5PM and 10PM. The results of EIS, photocurrent, PL and TRPL were combined to analyze the properties of the PM composites. The bare MIL-53(Fe) has a small arc radius but a high fluorescence intensity, which means more probability of charge recombination. Only when the proportion of PM composite is suitable can the photocatalysts have excellent electrochemical performance and high photodegradation efficiency.[42] Given the above, the improvement of photodegradation performance was related to the excellent charge separation and transfer in the heterojunction.

**3.5. Mechanism of 5PM Photocatalysts.** *3.5.1. Roles of Reactive Species.* While maintaining the high absorption of visible light and effective charge separation, it is also necessary that the photoexcited catalysts can effectively produce oxidation or reduction ability to act on the target. Different analytical methods are used here to demonstrate the type of heterojunction and active species, including radical trap experiments and electron spin resonance (ESR) analysis. In radical trap experiments, the scavengers of ·OH, ·$O_2^-$, and $h^+$ were the isopropanol (IPA), benzoquinone (BQ), and ethylenediaminetetraacetic acid disodium salt (EDTA), respectively. The results in Figure 7a show that $h^+$ play a major role in the degradation of pollutants, followed by ·OH, ·$O_2^-$. Moreover, the ESR analysis (Figure 7b,c) further proved the existence of ·OH and ·$O_2^-$ in the system. The obvious DMPO-·OH and DMPO-·$O_2^-$ signals were observed under visible light irradiation. In addition, the signal peaks increase with the extension of light duration. The results of ESR and radical trap experiments could prove that ·OH and ·$O_2^-$ were produced in photodegradation process, proving that the composite system has sufficient oxidation and reduction potential.

*3.5.2. Determination of Heterojunction Type.* Actually, the type-II heterojunction would lose a higher redox potential in the process of charge separation. The Z-scheme heterojunction has great potential in this respect among various heterojunction structures. Different from the type-II heterojunction, the Z-scheme heterojunction can ensure charge separation while retaining the strong redox capacity. In detail, the different direction of photogenerated charge transfer between the type-II heterojunction and the Z-scheme heterojunction was determined by the internal electric field. When two n-type


https://doi.org/10.1021/acsami.1c01308
ACS Appl. Mater. Interfaces XXXX, XXX, XXX−XXX

semiconductors are combined, the semiconductor contact surface would generate charge migration due to the difference of Fermi level. And then, the electrons will transfer from the semiconductor with a higher Fermi level to the semiconductor with a lower Fermi level to achieve the Fermi level to equilibrium.

According to the band structure (Figure 5e) and theory above, when PDI and MIL-53(Fe) were coupled, the electrons of PDI will transfer to MIL-53(Fe) near the contact interface. Then the energy band would bend in the opposite direction. Therefore, the charge distribution between the interfaces causes the internal electric field (IEF) (Figure S12). Here, the interaction between PDI and MIL-53(Fe) was further explained by the high-resolution XPS (HRXPS) spectra (Figure 7d and Figure S13). Fe was chosen as the element to be analyzed because it exists only in MIL-53(Fe). Comparing the Fe 2p patterns of samples in Figure 7d, it was found that the binding energy of 5PM was 0.3 eV lower than that of MIL-53(Fe) in the signal peak of Fe 3/2p. Furthermore, the binding energy is inversely related to the charge density. The area ratio of the $Fe^{2+}$ signal peak increased significantly, showing that the $Fe^{3+}$ of MIL-53(Fe) gets electrons and was reduced to divalent. All of the above indicated that the electrons transferred from PDI to MIL-53(Fe) in the composite sample. The direction of the polarization field was from PDI to MIL-53(Fe).

Besides, it is worth noting that ·OH was generated by $h^+$ oxidized water with an oxidation potential greater than 2.40 V vs NHE. Meanwhile $\cdot O_2^-$ was generated by $e^-$ reduced oxygen with a reduction potential less than −0.33 V vs NHE.[43] Combining the mechanisms, Figure S12 shows that the charge transfer mechanism of the Z-scheme heterojunction can produce both ·OH and $\cdot O_2^-$, while the type-II heterojunction was hard to do this at all. In conclusion, the heterojunction composed of PDI and MIL-53(Fe) was confirmed to be a Z-scheme structure.

*3.5.3. Possible Charge Transfer Mode and Degradation Path of 5PM.* In Figure 7e, the photogenerated charge transfer and photodegradation mechanism of the 5PM Z-scheme heterojunction were summarized and analyzed. Here, the reasons for charge transfer were mainly divided into two parts: Semiconductor characteristics (black frame) and IEF (blue frame).

Specifically, besides the charge separation caused by the Z-scheme heterojunction, the two semiconductors have their own direction of charge transfer under illumination. Here, a coordinating Z-scheme heterojunction mechanism in the PM photocatalyst was proposed. The optical transitions of MIL-53(Fe) can be assigned to ligand-to-metal charge transfer (LMCT). The organic ligand serves as an excitation part that receives illumination to generate charges. Then, the excited electrons transfer to the metal nodes.[44,45] The PDI molecule generates polarization due to its central perylene core and terminal carboxyl group. The photoexcited hole will transfer to the carboxyl group under the action of the intramolecular electric field, while the conjugated action of the perylene core would attract photoexcited electrons. As can be seen from the above, LMCT will cause the photogenerated electron of MIL-53(Fe) to transport from the BDC ligand to Fe-O chains. At the same time, the photogenerated hole of PDI prefers the terminal carboxyl group bonded to metal nodes. So, the electrons from PDI will recombine with the holes from MIL-53(Fe) on the composite interface. The charge transfer and recombination caused by the material's own characteristics are consistent with the role of a Z-scheme heterojunction. It makes the photogenerated electrons and holes with strong redox ability to retain on PDI and MIL, respectively, to participate in the subsequent reaction.

The possible intermediates and products of the TC-H degradation process were analyzed by the LC-MS technique. The possible pathway is presented in Figure S14. The $m/z$ = 445 corresponded to the molecular weight of TC-H. The intermediates with $m/z$ of 428 (Product 1) and 410 (Products 2 and 3) were identified as the dehydration and demethylation products. The products with $m/z$ of 477 (Product 4) and 459 (Product 5) were generated by the attack of ·OH. After irradiation for 30 min, products with $m/z$ of 340 (Product 6), 362 (Product 7), 262 (Product 8), 244 (Product 9), and 222 (Product 10) were assigned the further oxidation products.

**3.6. Photodegradation Reaction Mechanism.** To sum up, the photocatalytic mechanism of 5PM was discussed. Under illumination, the photogenerated charge transports under the polarization of PDI, LMCT of MIL-53(Fe), and the IEF. In the IEF of the 5PM Z-scheme photocatalyst, the photogenic electrons on MCB flowed from MIL-53(Fe) to PDI and compounded with the photogenic hole on PVB. This would leave the photogenic hole on MVB and the photogenic hole on PVB (MCB, MVB: conduction band and valence band of MIL-53(Fe). PCB, PVB: conduction band and valence band of PDI). Similarly, under the driving force of PDI's polarization, the photogenerated holes tend to move toward the terminal carboxyl group and then recombine with the photogenerated electrons. The photogenerated holes were excited to Fe-O chains near the composite interface; the electrons with strong reducing ability then accumulate on the PDI. So, the holes with strong oxidizing ability accumulate on the MIL-53(Fe). Subsequently, the electrons and holes on the surface of 5PM reacted with oxygen and water to form $\cdot O^{2-}$ and ·OH. Radicals and holes are the main active substances for the degradation process of TC-H. The effective charge separation between Z-scheme heterojunction also enhances the stability of the composite photocatalyst and extends the service time.

## 4. CONCLUSION

In conclusion, the highly efficient Z-scheme PM photocatalyst was constructed and researched. The TC-H photodegradation rate of 5PM within 30 min was close to 94.08%, which was 4 times that of PDI and 33 times that of MIL-53(Fe), respectively. The greatly enhanced photodegradation efficiency is due to the outstanding charge separation and redox capacity in 5PM. In terms of composite structure, PDI nanofibers were dispersed and fixed in MIL-53(Fe) with covalent bonds. The excellent charge transportation is related to a large contact interface and strong covalent bonding. In terms of a heterojunction, the formation of the Z-scheme heterojunction and the properties of semiconductor materials provide effective charge separation ability and strong redox potential. These factors result in the excellent pollutant removal ability and provide a new prospect for the performance improvement of MOFs composite photocatalysts.

## ■ ASSOCIATED CONTENT

### Supporting Information

The Supporting Information is available free of charge at https://pubs.acs.org/doi/10.1021/acsami.1c01308.



https://doi.org/10.1021/acsami.1c01308
ACS Appl. Mater. Interfaces XXXX, XXX, XXX−XXX

The SEM and TEM images. The 5PM control adsorption test. XPS, XRD, SEM, and FT-IR of used samples and prepared samples. The component's emission lifetimes and corresponding amplitudes of samples. The effects of different ions on the removal efficiency of 5PM. The EIS Nyquist plots of composites. The proposed transformation pathways of TC-H degradation (PDF)

## AUTHOR INFORMATION


### Corresponding Authors

**Yutang Liu** − *College of Environmental Science and Engineering, Hunan University, Changsha 410082, People's Republic of China; Key Laboratory of Environmental Biology and Pollution Control, Hunan University, Ministry of Education, Changsha 410082, People's Republic of China;* orcid.org/0000-0002-4975-364X; Email: yt_liu@hnu.edu.cn

**Lin Tang** − *College of Environmental Science and Engineering, Hunan University, Changsha 410082, People's Republic of China; Key Laboratory of Environmental Biology and Pollution Control, Hunan University, Ministry of Education, Changsha 410082, People's Republic of China;* orcid.org/0000-0001-6996-7955; Email: tanglin@hnu.edu.cn

### Authors

**Hui Chen** − *College of Environmental Science and Engineering, Hunan University, Changsha 410082, People's Republic of China; Key Laboratory of Environmental Biology and Pollution Control, Hunan University, Ministry of Education, Changsha 410082, People's Republic of China*

**Wengao Zeng** − *International Research Center for Renewable Energy, State Key Laboratory of Multiphase Flow in Power Engineering, Xi'an Jiaotong University, Xi'an 710049, China*

**Wanyue Dong** − *College of Environmental Science and Engineering, Hunan University, Changsha 410082, People's Republic of China; Key Laboratory of Environmental Biology and Pollution Control, Hunan University, Ministry of Education, Changsha 410082, People's Republic of China*

**Tao Cai** − *School of Resource & Environment and Safety Engineering, University of South China, Hengyang 421001, China*

**Juan Li** − *College of Environmental Science and Engineering, Hunan University, Changsha 410082, People's Republic of China; Key Laboratory of Environmental Biology and Pollution Control, Hunan University, Ministry of Education, Changsha 410082, People's Republic of China*

**Wenlu Li** − *College of Environmental Science and Engineering, Hunan University, Changsha 410082, People's Republic of China; Key Laboratory of Environmental Biology and Pollution Control, Hunan University, Ministry of Education, Changsha 410082, People's Republic of China*

Complete contact information is available at: https://pubs.acs.org/10.1021/acsami.1c01308

### Author Contributions

⊥H.C. and W.Z. contributed equally to this work.


### Notes

The authors declare no competing financial interest.

## ACKNOWLEDGMENTS

This work was supported by the National Natural Science Foundation of China (51872089 and 51672077), the Hunan Provincial Natural Science Foundation of China (2017JJ2026), the Key Laboratory of Jiangxi Province for Persistent Pollutants Control and Resources Recycle (Nanchang Hangkong University) (ES201880051), and the Funds for Innovative Province Construction of Hunan Province (2019-RS3012). The authors thank the National Supercomputing Center in Changsha for supporting this work.

## REFERENCES

(1) Dong, W.; Cai, T.; Liu, Y.; Wang, L.; Chen, H.; Zeng, W.; Li, J.; Li, W. Rapid Removal Of Organic Pollutants By A Novel Persulfate/Brochantite System: Mechanism And Implication. *J. Colloid Interface Sci.* **2021**, *585*, 400−407.

(2) Luo, J.; Fu, K.; Sun, M.; Yin, K.; Wang, D.; Liu, X.; Crittenden, J. C. Phase-Mediated Heavy Metal Adsorption From Aqueous Solutions Using Two-Dimensional Layered Mos2. *ACS Appl. Mater. Interfaces* **2019**, *11* (42), 38789−38797.

(3) Cai, T.; Liu, Y.; Wang, L.; Zhang, S.; Zeng, Y.; Yuan, J.; Ma, J.; Dong, W.; Liu, C.; Luo, S. Silver Phosphate-Based Z-Scheme Photocatalytic System With Superior Sunlight Photocatalytic Activities And Anti-Photocorrosion Performance. *Appl. Catal., B* **2017**, *208*, 1−13.

(4) Dong, W.; Liu, Y.; Zeng, G.; Zhang, S.; Cai, T.; Yuan, J.; Chen, H.; Gao, J.; Liu, C. Regionalized And Vectorial Charges Transferring Of Cd1-Xznxs Twin Nanocrystal Homojunctions For Visible-Light Driven Photocatalytic Applications. *J. Colloid Interface Sci.* **2018**, *518*, 156−164.

(5) Dhakshinamoorthy, A.; Asiri, A. M.; Garcia, H. Metal-Organic Framework (MOF) Compounds: Photocatalysts For Redox Reactions And Solar Fuel Production. *Angew. Chem., Int. Ed.* **2016**, *55* (18), 5414−45.

(6) Feng, C.; Deng, Y.; Tang, L.; Zeng, G.; Wang, J.; Yu, J.; Liu, Y.; Peng, B.; Feng, H.; Wang, J. Core-Shell Ag2CrO4/N-Gqds@G-C3N4 Composites With Anti-Photocorrosion Performance For Enhanced Full-Spectrum-Light Photocatalytic Activities. *Appl. Catal., B* **2018**, *239*, 525−536.

(7) Feng, C.; Tang, L.; Deng, Y.; Wang, J.; Liu, Y.; Ouyang, X.; Chen, Z.; Yang, H.; Yu, J.; Wang, J. Maintaining Stable LSPR Performance Of W18O49 By Protecting Its Oxygen Vacancy: A Novel Strategy For Achieving Durable Sunlight Driven Photocatalysis. *Appl. Catal., B* **2020**, *276*, 119167.

(8) Feng, C.; Tang, L.; Deng, Y.; Wang, J.; Tang, W.; Liu, Y.; Chen, Z.; Yu, J.; Wang, J.; Liang, Q. Synthesis Of Branched WO3@W18O49 Homojunction With Enhanced Interfacial Charge Separation And Full-Spectrum Photocatalytic Performance. *Chem. Eng. J.* **2020**, *389*, 124474.

(9) Meyer, K.; Ranocchiari, M.; Van Bokhoven, J. A. Metal Organic Frameworks For Photo-Catalytic Water Splitting. *Energy Environ. Sci.* **2015**, *8* (7), 1923−1937.

(10) Zhang, X.; Chen, J.; Jiang, S.; Zhang, X.; Bi, F.; Yang, Y.; Wang, Y.; Wang, Z. Enhanced Photocatalytic Degradation Of Gaseous Toluene And Liquidus Tetracycline By Anatase/Rutile Titanium Dioxide With Heterophase Junction Derived From Materials Of Institut Lavoisier-125(Ti): Degradation Pathway And Mechanism Studies. *J. Colloid Interface Sci.* **2021**, *588*, 122−137.

(11) Shi, X.; Zhang, X.; Bi, F.; Zheng, Z.; Sheng, L.; Xu, J.; Wang, Z.; Yang, Y. Effective Toluene Adsorption Over Defective Uio-66-NH2: An Experimental And Computational Exploration. *J. Mol. Liq.* **2020**, *316*, 113812.

(12) Yang, Y.; Zheng, Z.; Ji, W.; Xu, J.; Zhang, X. Insights To Perfluorooctanoic Acid Adsorption Micro-Mechanism Over Fe-Based Metal Organic Frameworks: Combining Computational Calculation With Response Surface Methodology. *J. Hazard. Mater.* **2020**, *395*, 122686.



https://doi.org/10.1021/acsami.1c01308
ACS Appl. Mater. Interfaces XXXX, XXX, XXX−XXX

(13) Hyok Ri, S.; Bi, F.; Guan, A.; Zhang, X. Manganese-Cerium Composite Oxide Pyrolyzed From Metal Organic Framework Supporting Palladium Nanoparticles For Efficient Toluene Oxidation. *J. Colloid Interface Sci.* **2021**, *586*, 836−846.
(14) Murray, L. J.; Dinca, M.; Long, J. R. Hydrogen Storage In Metal-Organic Frameworks. *Chem. Soc. Rev.* **2009**, *38* (5), 1294−314.
(15) Qiu, J.; Zhang, X.; Feng, Y.; Zhang, X.; Wang, H.; Yao, J. Modified Metal-Organic Frameworks As Photocatalysts. *Appl. Catal., B* **2018**, *231*, 317−342.
(16) Wang, C.-C.; Li, J.-R.; Lv, X.-L.; Zhang, Y.-Q.; Guo, G. Photocatalytic Organic Pollutants Degradation In Metal-Organic Frameworks. *Energy Environ. Sci.* **2014**, *7* (9), 2831−2867.
(17) Liang, Z.; Qu, C.; Guo, W.; Zou, R.; Xu, Q. Pristine Metal-Organic Frameworks And Their Composites For Energy Storage And Conversion. *Adv. Mater.* **2017**, *30*, 1702891.
(18) Cai, T.; Liu, Y.; Wang, L.; Zhang, S.; Ma, J.; Dong, W.; Zeng, Y.; Yuan, J.; Liu, C.; Luo, S. Dark Deposition" Of Ag Nanoparticles On Tio2: Improvement Of Electron Storage Capacity To Boost "Memory Catalysis" Activity. *ACS Appl. Mater. Interfaces* **2018**, *10* (30), 25350−25359.
(19) De Yoreo, J. J.; Gilbert, P. U. P. A.; Sommerdijk, N. A. J. M.; Penn, R. L.; Whitelam, S.; Joester, D.; Zhang, H.; Rimer, J. D.; Navrotsky, A.; Banfield, J. F.; Wallace, A. F.; Michel, F. M.; Meldrum, F. C.; Cölfen, H.; Dove, P. M. Crystallization By Particle Attachment In Synthetic, Biogenic, And Geologic Environments. *Science* **2015**, *349*, aaa6760.
(20) Wang, J.; Shi, W.; Liu, D.; Zhang, Z.; Zhu, Y.; Wang, D. Supramolecular Organic Nanofibers With Highly Efficient And Stable Visible Light Photooxidation Performance. *Appl. Catal., B* **2017**, *202*, 289−297.
(21) Chen, H.; Liu, Y.; Cai, T.; Dong, W.; Tang, L.; Xia, X.; Wang, L.; Li, T. Boosting Photocatalytic Performance In Mixed-Valence MIL-53(Fe) By Changing Fe(II)/Fe(III) Ratio. *ACS Appl. Mater. Interfaces* **2019**, *11* (32), 28791−28800.
(22) Zeng, W.; Cai, T.; Liu, Y.; Wang, L.; Dong, W.; Chen, H.; Xia, X. An Artificial Organic-Inorganic Z-Scheme Photocatalyst WO3@Cu@PDI Supramolecular With Excellent Visible Light Absorption And Photocatalytic Activity. *Chem. Eng. J.* **2020**, *381*, 122691.
(23) Biemmi, E.; Scherb, C.; Bein, T. Oriented Growth Of The Metal Organic Framework Cu3(BTC)2(H2O)3ηXh2o Tunable With Functionalized Self-Assembled Monolayers. *J. Am. Chem. Soc.* **2007**, *129* (26), 8054−8055.
(24) Tian, H.; Araya, T.; Li, R.; Fang, Y.; Huang, Y. Removal Of MC-LR Using The Stable And Efficient MIL-100/MIL-53 (Fe) Photocatalyst: The Effect Of Coordinate Immobilized Layers. *Appl. Catal., B* **2019**, *254*, 371−379.
(25) Liu, N.; Huang, W.; Zhang, X.; Tang, L.; Wang, L.; Wang, Y.; Wu, M. Ultrathin Graphene Oxide Encapsulated In Uniform MIL-88A(Fe) For Enhanced Visible Light-Driven Photodegradation Of Rhb. *Appl. Catal., B* **2018**, *221*, 119−128.
(26) Liu, N.; Huang, W.; Tang, M.; Yin, C.; Gao, B.; Li, Z.; Tang, L.; Lei, J.; Cui, L.; Zhang, X. In-Situ Fabrication Of Needle-Shaped MIL-53(Fe) With 1T-Mos2 And Study On Its Enhanced Photocatalytic Mechanism Of Ibuprofen. *Chem. Eng. J.* **2019**, *359*, 254−264.
(27) Zhou, G.; Wu, M.-F.; Xing, Q.-J.; Li, F.; Liu, H.; Luo, X.-B.; Zou, J.-P.; Luo, J.-M.; Zhang, A.-Q. Synthesis And Characterizations Of Metal-Free Semiconductor/Mofs With Good Stability And High Photocatalytic Activity For H 2 Evolution: A Novel Z-Scheme Heterostructured Photocatalyst Formed By Covalent Bonds. *Appl. Catal., B* **2018**, *220*, 607−614.
(28) Van Vleet, M. J.; Weng, T.; Li, X.; Schmidt, J. R. In Situ, Time-Resolved, And Mechanistic Studies Of Metal-Organic Framework Nucleation And Growth. *Chem. Rev.* **2018**, *118* (7), 3681−3721.
(29) Cai, T.; Zeng, W.; Liu, Y.; Wang, L.; Dong, W.; Chen, H.; Xia, X. A Promising Inorganic-Organic Z-Scheme Photocatalyst Ag3PO4/PDI Supermolecule With Enhanced Photoactivity And Photostability For Environmental Remediation. *Appl. Catal., B* **2020**, *263*, 118327.
(30) Bian, Z.; Tachikawa, T.; Zhang, P.; Fujitsuka, M.; Majima, T. A Nanocomposite Superstructure Of Metal Oxides With Effective Charge Transfer Interfaces. *Nat. Commun.* **2014**, *5*, 3038.
(31) Whitfield, T. R.; Wang, X.; Liu, L.; Jacobson, A. J. Metal-Organic Frameworks Based On Iron Oxide Octahedral Chains Connected By Benzenedicarboxylate Dianions. *Solid State Sci.* **2005**, *7* (9), 1096−1103.
(32) Zhang, K.; Wang, J.; Jiang, W.; Yao, W.; Yang, H.; Zhu, Y. Self-Assembled Perylene Diimide Based Supramolecular Heterojunction With Bi2WO6 For Efficient Visible-Light-Driven Photocatalysis. *Appl. Catal., B* **2018**, *232*, 175−181.
(33) Kumar, R.; Raut, D.; Ramamurty, U.; Rao, C. Remarkable Improvement In The Mechanical Properties And CO 2 Uptake Of Mofs Brought About By Covalent Linking To Graphene. *Angew. Chem., Int. Ed.* **2016**, *55*, 7857−7861.
(34) Ai, L.; Zhang, C.; Li, L.; Jiang, J. Iron Terephthalate Metal-Organic Framework: Revealing The Effective Activation Of Hydrogen Peroxide For The Degradation Of Organic Dye Under Visible Light Irradiation. *Appl. Catal., B* **2014**, *148*−*149*, 191−200.
(35) Huang, Q.; Hu, Y.; Pei, Y.; Zhang, J.; Fu, M. In Situ Synthesis Of Tio2@NH2-MIL-125 Composites For Use In Combined Adsorption And Photocatalytic Degradation Of Formaldehyde. *Appl. Catal., B* **2019**, *259*, 118106.
(36) Wang, L.; Xie, L.; Zhao, W.; Liu, S.; Zhao, Q. Oxygen-Facilitated Dynamic Active-Site Generation On Strained Mos2 During Photo-Catalytic Hydrogen Evolution. *Chem. Eng. J.* **2021**, *405*, 127028.
(37) Chiu, Y.-H.; Hsu, Y.-J. Au@Cu 7 S 4 Yolk@Shell Nanocrystal-Decorated Tio 2 Nanowires As An All-Day-Active Photocatalyst For Environmental Purification. *Nano Energy* **2017**, *31*, 286−295.
(38) Bai, S.; Jiang, J.; Zhang, Q.; Xiong, Y. Steering Charge Kinetics In Photocatalysis: Intersection Of Materials Syntheses, Characterization Techniques And Theoretical Simulations. *Chem. Soc. Rev.* **2015**, *44* (10), 2893−939.
(39) Zhang, C.; Ai, L.; Jiang, J. Solvothermal Synthesis Of MIL-53(Fe) Hybrid Magnetic Composites For Photoelectrochemical Water Oxidation And Organic Pollutant Photodegradation Under Visible Light. *J. Mater. Chem. A* **2015**, *3* (6), 3074−3081.
(40) Yang, Z.; Xu, X.; Liang, X.; Lei, C.; Wei, Y.; He, P.; Lv, B.; Ma, H.; Lei, Z. MIL-53(Fe)-Graphene Nanocomposites: Efficient Visible-Light Photocatalysts For The Selective Oxidation Of Alcohols. *Appl. Catal., B* **2016**, *198*, 112−123.
(41) Dong, W.; Liu, Y.; Zeng, G.; Cai, T.; Shao, L.; Chen, H.; Zeng, W.; Xia, X. Crystal Phase Engineering Zn0.8Cd0.2S Nanocrystals With Twin-Induced Homojunctions For Photocatalytic Nitrogen Fixation Under Visible Light. *J. Photochem. Photobiol., A* **2020**, *401*, 112766.
(42) Tian, H.; Wu, H.; Fang, Y.; Li, R.; Huang, Y. Hydrothermal Synthesis Of M-Bivo4/T-Bivo4 Heterostructure For Organic Pollutants Degradation: Insight Into The Photocatalytic Mechanism Of Exposed Facets From Crystalline Phase Controlling. *J. Hazard. Mater.* **2020**, *399*, 123159.
(43) Low, J.; Jiang, C.; Cheng, B.; Wageh, S.; Al-Ghamdi, A. A.; Yu, J. A Review Of Direct Z-Scheme Photocatalysts. *Small Methods* **2017**, *1* (5), 1700080.
(44) Alvaro, M.; Carbonell, E.; Ferrer, B.; Llabres I Xamena, F. X.; Garcia, H. Semiconductor Behavior Of A Metal-Organic Framework (MOF). *Chem. - Eur. J.* **2007**, *13* (18), 5106−12.
(45) Du, J.-J.; Yuan, Y.-P.; Sun, J.-X.; Peng, F.-M.; Jiang, X.; Qiu, L.-G.; Xie, A.-J.; Shen, Y.-H.; Zhu, J.-F. New Photocatalysts Based On MIL-53 Metal-Organic Frameworks For The Decolorization Of Methylene Blue Dye. *J. Hazard. Mater.* **2011**, *190* (1), 945−951.


https://doi.org/10.1021/acsami.1c01308
ACS Appl. Mater. Interfaces XXXX, XXX, XXX−XXX